Check for updates

Utilising acoustic techniques to improve understanding of the formation process in sodium-ion batteries

Arthur Fordham, [ID] †[a,c,f] Dylan Wee,†[b,c] Rhodri E. Owen,[c,g] Tongjun Luo,[d,f] Roksana Jackowska, [ID] [c,e] Tianqi Jia,[d] Yan Zheng,[d] Emma Kendrick, [ID] [c,e] Wesley M. Dose, [ID] [d,f] Dan J. L. Brett,[h] Paul R. Shearing,[c,i] James B. Robinson [ID] *[a,c,g] and Rhodri Jervis [ID] *[a,c,g]

Sodium-ion batteries (NIBs) offer a more sustainable and cost-effective alternative to lithium-ion batteries (LIBs), but challenges related to the formation process and the impact of electrolyte additives on the solid electrolyte interphase (SEI) remain underexplored. Moreover, current SEI diagnostic tools are often prohibitively expensive, limiting broader adoption. This work investigates *operando*, non-invasive acoustic techniques – combining passive acoustic emission (AE) and active ultrasonic testing (UT) – to monitor SEI formation in $NaMn_{0.39}Fe_{0.31}Ni_{0.22}Zn_{0.08}O_2$/hard carbon (HC) pouch cells using four electrolyte formulations: a baseline of 1 M $NaPF_6$ in 1 : 1 EC : DMC, and three with additives (5 wt% fluoroethylene carbonate (FEC), vinylene carbonate (VC), or both). Identical formation protocols were applied, with SEI evolution monitored *via* AE and UT, and correlated with a range of characterisation techniques including *operando* gas volume measurements, three-electrode dQ/dV analysis, and X-ray CT. Bespoke machine learning algorithms were developed to interpret acoustic signals. Results revealed incomplete SEI passivation across all formulations, evidenced by ongoing gas evolution and high irreversible capacity loss after three formation cycles. The behaviour in formation was reflected in the long-term cycling results: FEC delivered the best performance, VC alone was less effective, and cells without additives performed worst. These findings highlight the importance of tailored additive selection when using $NaPF_6$ in NIBs. This work demonstrates that AE and UT provide a viable, low-cost solution for real-time SEI monitoring, offering mechanistic insight previously accessible only through more complex and costly techniques.

Broader context

Sodium-ion batteries (NIBs) are emerging as a low-cost, sustainable alternative to lithium-ion systems, but their widespread commercialisation requires detailed understanding of solid electrolyte interphase (SEI) formation, a process central to stability and efficiency. Traditional diagnostic tools for SEI characterisation are costly, *ex situ*, and often restricted to laboratory use, slowing progress in scaling NIBs for industrial applications. This work demonstrates the use of *operando* acoustic techniques – acoustic emission (AE) and ultrasonic testing (UT) – as low-cost, non-invasive methods to monitor SEI formation and gas evolution in real time. Applied to NIBs with different electrolyte additives and complemented by additional characterisation methods, these techniques reveal that conventional formation protocols leave the SEI incomplete, with acoustic signals directly correlating to gas generation and interfacial instability. Importantly, fluoroethylene carbonate (FEC) is identified as the most effective additive of those studied here for improving capacity retention, while cells without additives exhibit poor performance. These advances highlight acoustic monitoring as a scalable diagnostic platform that can accelerate the understanding of the formation process, reduce manufacturing costs, and improve the reliability of sodium-ion batteries, thereby impacting the broader field of sustainable energy storage.

[a]Electrochemical Innovation Lab, Department of Chemical Engineering, University College London, London, WC1E 7JE, UK. E-mail: j.b.robinson@ucl.ac.uk, rhodri.jervis@ucl.ac.uk
[b]Department of Mechanical Engineering, Imperial College London, London, SW7 2BX, UK
[c]The Faraday Institution, Quad One, Harwell Science and Innovation Campus, Didcot, UK, OX11 0RA, UK
[d]School of Chemistry, University of Sydney, Camperdown, NSW 2006, Australia
[e]School of Metallurgy and Materials, University of Birmingham, Birmingham, B15 2SE, UK
[f]School of Chemistry, University of New South Wales, Sydney, NSW 2052, Australia
[g]Advanced Propulsion Lab, Marshgate, 7 Sidings Street, University College London, London, E20 2AE, UK
[h]Prosemino, Unit 2, Paper Yard, Quebec Way, London SE16 7LG
[i]ZERO Institute, Holywell House, Osney Mead, University of Oxford, Oxford, OX2 0ES, UK
†These authors made equal contribution.

Introduction

Battery technology plays a crucial role in driving the transition towards a more electrified future. However, as lithium-ion batteries (LIBs) become more widely adopted for use in different conditions and applications, diversifying the supply chain and finding alternative chemistries suitable for other applications, such as stationary storage, is becoming ever more important.[1]

Sodium-ion batteries (NIBs) are a leading alternative to lithium-ion batteries (LIBs), driven by the vastly greater abundance of sodium – around 23 000 ppm in the Earth's crust compared to just 20 ppm for lithium.[2] Unlike lithium, which is primarily mined in Australia and South American salars and largely processed in China,[3] sodium can be sourced from widely available resources such as seawater and salt mines, easing supply chain concerns and improving long-term sustainability.[4] Given the chemical similarities between sodium and lithium, the key working principle behind NIBs and their manufacturing methods remain largely similar to LIBs,[5] making NIBs an attractive alternative to LIBs and a relatively drop-in technology to existing production lines. NIBs may also offer safety advantages when compared to LIBs. Whereas discharging to 0 V in a LIB would result in electrochemical dissolution of Cu (negative electrode current collector) and poor SEI stability, causing capacity loss and potentially internal damage to the cell, NIBs have been shown to continue performing without issues after discharge to 0 V.[6,7] NIB cells have also been shown to undergo a less extreme thermal runaway event in the case of failure than a range of LIB chemistries including $LiCoO_2$ and $Li_{1-x}Ni_xMn_yCo_zO_2$.[6–9]

The formation cycle plays a key role in the production processes of LIBs and NIBs.[10] During this first charge and discharge cycle, the solid-electrolyte interphase (SEI) layer grows and develops on the surface of the hard carbon negative electrode following an electrochemical reduction reaction involving both the organic and inorganic components of the electrolyte. The SEI is crucial to the stability of the battery as it is a passivating film that is ionically conductive and allows Na^+ transport, while also being electronically insulating, thereby preventing further electrolyte decomposition. The formation cycle is an essential step in controlling the performance of the cell, ensuring its longevity, uniform capacity and safety; however, it is also the costliest step in the manufacturing process. Compared to the $2.2 per kWh required for electrode processing, the electrode wetting/formation cycle was estimated to cost $7.5 per kWh for LIBs,[11] and is expected to be similar for NIBs. Despite its economic and functional importance, the formation cycle is often overlooked in battery research, which tends to focus on improving cell chemistry. This is largely because formation is highly specific to the electrode materials, electrolyte composition, and additives used. Its complexity, along with the need for specialised techniques and moisture/oxygen-free conditions, makes it difficult to study in academic settings. As a result, the process remains proprietary for LIBs, with even less information available for NIBs.

Amongst the various methods used to observe and understand the formation of the SEI, acoustic techniques have gained increased attention in recent years due to their non-invasive nature and ability to record *operando* measurements at a low cost.[12] Two main forms of acoustic techniques have been employed to analyse degradation in batteries: Acoustic Emission (AE) and Ultrasonic Testing (UT). AE is a passive technique that 'listens' for significant acoustic events that cross a pre-specified amplitude threshold. As batteries are cycled, they experience mechanical stresses and undergo chemical processes that result in gas formation and cracking, all of which release pressure waves that propagate through the material within the cell.[12] These waves are then identified by a piezoelectric sensor affixed to the surface of a cell, before being amplified, filtered, processed and analysed to determine the possible origins of the acoustic event.[13] Pulse-echo UT is an active acoustic method where a piezoelectric transducer sends ultrasonic pulses into a material and detects returning echoes from internal surfaces. Applied to a battery surface, changes in the captured waves during cycling reveal structural evolution and degradation inside the cell.[12]

Acoustic techniques have been useful in studying the internal processes within LIBs such as gas evolution, cracking, delamination, and electrode volume changes.[12] Beganovic *et al.* developed a model to use AE measurements, to validate its utility in estimating the state of health (SOH) and remaining useful life (RUL) of LIBs.[14] Choe *et al.* studied AE waveforms in more detail and deduced the presence of two different types of waveforms. Type 1 AE signals had a shorter waveform, higher amplitude and higher frequencies between the range of 121–160 kHz and attributed to micro-cracking in the negative electrode. Type 2 signals had longer durations, lower amplitudes and stayed within the lower frequency range of 81–120 kHz and were attributed to gas bubble evolution during SEI formation.[15] This finding was used by Matsuo *et al.* who compared the Type 1 AE waveforms with signals from mechanically induced fracture during a Vickers indentation test, and Type 2 waveforms with acoustic signals labelled as "*hits*" from gas evolution in hydrolysis, to develop a model identifying the ongoing degradation mechanisms in the LIB.[13] Our work further developed this waveform classification by integrating supervised machine learning algorithms to classify the acoustic signals produced from degradation mechanisms and gassing in commercial 21 700 cylindrical cells.[16]

Hsieh *et al.* demonstrated the ability of UT to estimate the state of charge (SOC) and SOH of LIBs.[17] Bommier *et al.* then developed this method further and showed a temporary loss of acoustic signal associated with significant gassing of a LIB, proving the potential for UT in offering insights on SEI formation.[18] Deng *et al.* and Guo *et al.* also explored the robustness of pulse-echo UT in observing the real-time processes ongoing within a LIB, such as the wetting process of pouch cells and gassing within the cell.[19,20] Zhang *et al.* developed the technique by using UT methods to improve the electrode drying process for enhanced battery manufacturing.[21]

Based on the similarity of the components and cell structure in LIBs and NIBs, Majasan *et al.* highlighted that acoustic techniques for NIBs would likely be similar to that for LIBs,[12]

but limited work has been published to support this hypothesis. Dreyer *et al.* investigated the relationship between the configurational entropy of the positive electrode and the AE hits in NIBs, specifically investigating the fracture and delamination within the cell, meaning that more emphasis was placed on acoustic hits of higher frequencies, such as Type 1 waveforms.[22] Gassing in the cell was observed to be an insignificant contributor to acoustic hits beyond the initial formation cycle of NIBs, a behaviour that was observed by Schweidler *et al.* in LIBs.[23]

Since gassing can be easily detected through acoustic methods, recent research has focused on understanding the gassing that occurs during the formation cycle due to SEI growth. Gaining a deeper understanding of the SEI is crucial, as the stability of this layer significantly influences battery performance. There are notable differences in the SEI between LIBs and NIBs. Mogensen *et al.* found that NIBs had poorer capacity retention and tended to undergo self-discharge to a larger extent than LIBs, attributing these effects to a more soluble SEI in NIBs than LIBs.[24] This finding was supported by Song *et al.* who concluded that the SEI constituents in NIBs such as Na_2CO_3 and NaF had much lower stability and higher solubility when compared to their lithium-ion equivalents (Li_2CO_3 and LiF).[25] Zhang *et al.* and Hijazi *et al.* both observed that the increased solubility of SEI constituents in the sodium electrolyte resulted in increased effects of crosstalk between the positive and negative electrodes.[26,27] Hijazi *et al.* also analysed the gassing of NIBs using a two-compartment pouch bag to separate the positive and negative electrodes. They recorded gas evolution mainly at the positive electrode and evidence of gas consumption at the negative *via* crosstalk.[26] This conclusion was backed up by the hypothesis that the sodiated hard carbon was at a sufficiently low voltage to allow the reduction of gaseous products such as CO_2 generated at the positive electrode, like mechanisms seen in LIBs.[28,29] However, this result occurs post-charging and is distinct from gas generation during SEI formation, which is the focus of this study.

The stability and homogeneity of the SEI is heavily dependent on the electrolyte additives, which also play a key role in contributing to gaseous products evolved during formation of the cell. While significant research has explored the role of electrolyte additives in layered LIBs, there has been limited research for NIBs. Nonetheless, Ye *et al.* explored the effect of $NaPF_6$ and sodium bis(fluorosulfonyl)imide (NaFSI) electrolytes on the production of gas during the ageing process of NIBs. They reported that the use of NaFSI, instead of $NaPF_6$, substantially reduced the amount of gas generated, due to the presence of PET tape in the cell which reacts with $NaPF_6$ but not with NaFSI.[30] Further work by Yang *et al.* employed sodium difluorophosphate (NaDFP) in hard carbon negative electrode half-cells, improving their cycling performance and suppressing the impedance increase by forming an effective SEI.[31] However, its effectiveness in full cells was not explored. Hijazi *et al.* experimented with other additives including VC, NaDFP, prop-1-ene-1,3-sultone (PES) and 1,3,2-dioxathiolane-2,2-dioxide (DTD) with both $NaPF_6$ and NaFSI. They concluded that the PES, NaDFP and DTD additives caused negligible gassing during formation

as compared to their control cells without additives, whereas VC additive generated some gas but still much less than the control.[26] VC as an electrolyte additive in LIBs has been shown to allow the formation of a more stable SEI as indicated by a high first-cycle coulombic efficiency (FCE).[26,32–34]

The effects of fluorine-based additives were also investigated in NIBs. Fluoroethylene carbonate (FEC) was used as an additive in NIBs with sodium perchlorate ($NaClO_4$) electrolyte by Song *et al.* and this resulted in the cell capacity reducing by more than half compared to cells without additives present.[25] This finding was supported by Wang *et al.* who noted that the SEI was less ionically conductive compared to a FEC-free electrolyte, leading to a lower cell capacity. In return, the addition of FEC to the same $NaClO_4$ electrolyte offered a significantly longer lifespan.[35] Vogt *et al.* observed that the use of FEC preserved the polyvinylidene difluoride (PVDF) binder in cells by providing a fluorine source for SEI formation.[36] Hydrogen fluoride (HF) evolved upon decomposition of FEC could, however, be detrimental to SEI stability and ion transport function of NIBs, an effect seen in LIBs.[37,38]

Understanding of the SEI in NIBs remains limited, as reflected in current literature. For the first time, this study systematically explores how acoustic techniques can be correlated with other characterisation methods – including operando gas volume measurements, X-ray CT, SEM, and various electrochemical analyses – to enhance insight into SEI formation of NIBs. Passive acoustic emission and ultrasonic testing already defined so can just write AE and UT, combined with machine learning, were employed to monitor the formation cycle in NIBs with different electrolyte additives. The work focuses on $NaMn_{0.39}Fe_{0.31}Ni_{0.22}Zn_{0.08}O_2$/hard carbon (HC) pouch cells using four electrolyte formulations: a baseline 1 M $NaPF_6$ in 1:1 EC:DMC, and three variants with 5 wt% additives – fluoroethylene carbonate (FEC), vinylene carbonate (VC), and a combination of both (FEC + VC). These formulations were selected due to their frequent use and commercial relevance in the NIB industry.[25–27,39] Acoustic techniques were used to examine how these electrolytes affect SEI formation during the formation cycle and over long-term cycling. Results were correlated with cycle life and validated through impedance analysis. This study demonstrates that low-cost, non-invasive, and non-destructive acoustic methods can be effectively applied to full cells, highlighting their industrial potential. Unlike conventional SEI characterisation tools, which are often limited to laboratory use due to scalability issues, acoustic techniques offer a promising route for *operando*, scalable monitoring in real-world applications.

Experimental methodology

Acoustic emission

Acoustic Emission (AE) signals were monitored using a piezoelectric sensor (S9208; Mistras NDT, UK) with a 25 mm diameter and height, and a flat frequency response over 20–1000 kHz. A couplant gel (Olympus D12) was applied between the

transducer and cell to ensure good acoustic transmission. The transducer was mounted in a custom holder atop the cell, which was placed inside a sound-insulated chamber. The same coupling gel and sensor mounting procedure were used for all experiments, with identical pressure applied by placing a 0.5 kg free mass on top of the rig during the experiments (Fig. 1). This ensured consistent acoustic coupling and minimised variations in signal strength between tests. The AE cable was connected to a 26 dB pre-amplifier (Mistras IL-LP-WS; 100–1000 kHz), a digital AE node (USB-Node; Mistras), and a computer with AEwin acoustic signal processing software (1283-7001-ACQ-KEY-SW AEwin for USB software) and a (USB key-based) acquisition licence. During cycling, acoustic signals exceeding a 28 dB threshold were filtered, amplified, and recorded by the AEWin software, labelled as *"hits"*.[16]

Ultrasonic time-of-flight

Active pulse-echo Time-of-Flight (ToF) measurements were performed using a 5 MHz, 6 mm diameter ultrasonic transducer (Olympus M110-RM), mounted beside the AE transducer (Fig. 1). The transducer was excited once per minute using a Panametrics 5052PR pulse-receiver, with responses recorded *via* a PicoScope oscilloscope. Signals were filtered, scaled, and processed using a custom Python script to analyse peak amplitude and shape. The ToF measurements aimed to track signal changes caused by gas evolution during the formation cycle.


Fig. 1 Schematic of the experimental set up. Figure outlines the electrical connections to the maccor battery cyclers, the Li-Fun cell, the ultrasonic transducer, acoustic emission transducer, and cell holder.

Cell details and filling protocol

Commercial-grade 225 mAh sodium-ion pouch cells (Li-Fun Technology) with $NaMn_{0.39}Fe_{0.31}Ni_{0.22}Zn_{0.08}O_2$ positive electrode and hard carbon negative electrodes were used. The positive electrode material contained an active material loading of 95.2%, a capacity of 140 mAh g^{-1}, a coating weight of 16.0 mg cm^{-2}, and a press density of 2.9 g cc^{-1}. The hard carbon electrode contained a 95.5% loading of active material, 280 mAh g^{-1} capacity, 9.55 mg cm^{-2} coating weight, and 0.8 g cc^{-1} press density. The separator consists of 16 μm PE plus a 4 μm ceramic layer. The cells are balanced with a positive-to-negative electrode capacity ratio (cell balance) of 1.2, meaning that the excess positive electrode capacity ensures full utilisation of the HC hard carbon while preventing sodium plating during cycling.

Cells, purchased dry, were cut open, vacuum-dried at 100 °C for ~12 hours (BUCHI-4 B-585), then transferred to an argon-filled glovebox (MBraun). Four electrolytes were tested: a baseline 1.0 M $NaPF_6$ in 1 : 1 EC : DMC, and three variants with 5 wt% FEC, 5 wt% VC, or 5 wt% FEC + VC. Each cell was filled with 1.0 mL electrolyte, vacuum-sealed at −70 kPa (Audion Audiovac) and heat-sealed at 215 °C (MSK-140). Finally, cells were mounted in custom compression rigs equipped with springs providing a pressure of 0.1 MPa and subsequently placed in a Maccor temperature chamber (MTC-020) maintained at 25 °C for a minimum of 12 h to ensure complete electrolyte wetting.

Formation protocol

After sufficient wetting (12 hours), the cells were removed from the temperature chambers and connected to a second custom holder designed to maintain equal pressure on two acoustic transducers (Fig. 1), ensuring consistent positioning on top of the cell. Couplant (Olympus D-12) was applied between the transducer and the cell to optimise ultrasonic contact. The holder was then placed inside the acoustic chamber lined with five layers of foam to insulate frequencies between 10–500 kHz, removing background noise in the range of interest for this study. The cell was then connected to a Biologic SP-300 potentiostat and subjected to a formation protocol. Each cell was charged at C/20 to 3.8 V with constant current and held at a constant voltage until the current dropped to C/200, before being discharged to 1.5 V. This process is then repeated at a C/5 rate for two additional cycles under ambient conditions, using the same voltage window. Each cycle includes constant current charge/discharge and a constant voltage step at the end of the charge, maintained until the current drops to C/50. All electrolytes (no additive, FEC, VC, and FEC + VC) were prepared simultaneously to ensure consistency and prevent decomposition. Each condition was tested sequentially using the same acoustic transducers, and the procedure was repeated twice for reproducibility.

Three-electrode measurements

PAT-Cells (EL-CELL) were used for three-electrode measurements during the formation cycle of each sample using a pre-assembled PEEK sleeve with sodium metal reference (EL-CELL). Electrodes were extracted from pristine dry LiFUN pouch cells, cleaned on
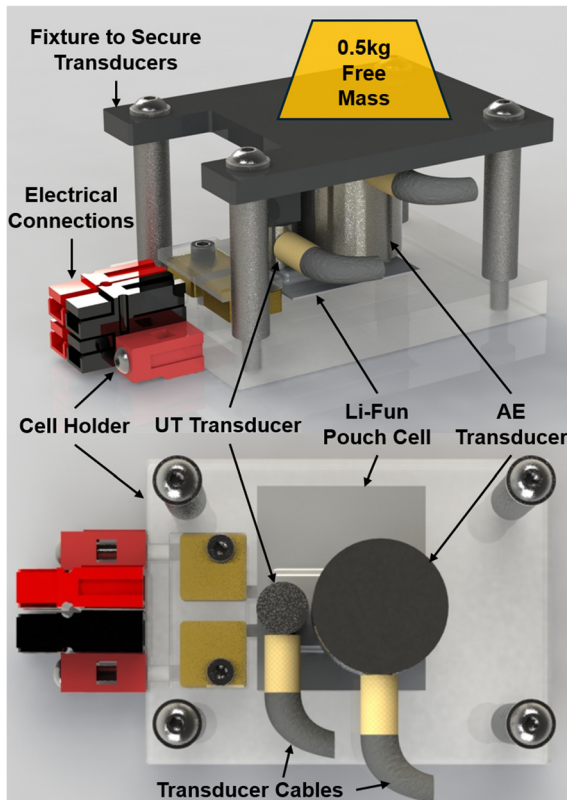
one side with NMP to expose the current collector, dried at 120 °C, and cut into discs (18 mm). Electrode discs (sodium layered positive and hard carbon negative electrode) were placed inside the EL-CELL along with 80 μl of each respective electrolyte. A schematic diagram of the PAT-Cells is shown in Fig. S24.

Cycling protocol

After formation, cells were returned to the glovebox, degassed using ceramic scissors, resealed, and reconnected to the acoustic holder (Fig. 1) before being placed back in the acoustic chamber. Each cell was cycled for 400 cycles (1.5–3.8 V) using C/3 charge and CV hold until C/30, with even pressure applied across the stack. Cells were initially cycled between 1.5–4.0 V during formation based on manufacturer recommendations. However, subsequent testing (shown in Fig. S6) revealed that UCVs above 3.8 V led to accelerated degradation, confirming that 3.8 V is optimal for capacity retention. Acoustic transducers monitored gas evolution and other internal processes. Parallel cells with identical electrolytes were also degassed and tested on a NOVONIX ultra-high precision coulometry (UHPC) system. The NOVONIX setup, with thermal chambers and dual temperature sensing, ensured 25 °C stability and coulombic efficiency measurements with <20 ppm precision. These cells underwent 500 cycles (C/3 charge/discharge between 1.5–3.8 V with a CV hold at 3.8 V until a current limit of C/30 was reached) to evaluate long-term performance and identify links between acoustic activity and formation cycle quality.

Electrochemical impedance spectroscopy

Alongside UHPC testing, repeat measurements were conducted using a Bio-Logic BCS-126 battery cycler. Potentiostatic electrochemical impedance spectroscopy (PEIS) was performed to assess the solid electrolyte interphase resistance (R_{SEI}) and total cell resistance after the formation cycles prior to cycling and every 50 cycles thereafter. Measurements were taken at 2.9, 3.3, and 3.7 V during C/10 cycling, following a 180 minute rest to ensure equilibrium. Tests were carried out at 25 °C using a 5 mV perturbation over a 10 mHz–10 kHz frequency range. Data were fitted using the ZFit function in EC-Lab®, based on the equivalent circuit model shown in Fig. S1.

Operando gas volume measurement

To quantify gas volume evolution during cycling, measurements were employed using an apparatus based on the Archimedes principle developed by Aiken and Self *et al.*[40–42] The experimental setup involved a HR-100AZ density balance with a suspended cell submerged in mineral oil (density: 0.83 g mL^{-1}) with thin Gamry 1000 potentiostat cables connected to the cell. A mass reading was recorded every 5 seconds using RS Weight software, while electrochemical readings were captured with Gamry Framework. The formation protocol mirrored the acoustic measurements.

X-ray computed tomography

X-ray computed tomography (CT) was performed on each cell to provide a clear, visual representation of each cell's internal structure, allowing for the assessment of gas generation during formation, as well as other degradation effects.[43] Each cell was scanned three times using a lab-based X-ray CT system (Nikon XT 225, Nikon Metrology, UK): before the formation cycle, immediately after, and after 500 cycles. Cells were secured in a custom 3D-printed holder. Scan parameters were 150 kV, 150 μA (22.5 W), using a cone beam with a tungsten target, 1 s exposure per projection, and a 0.5 mm Sn filter. Each tomogram comprised 3185 projections over 360°, taking ~25 min. Data were reconstructed in Nikon CT Pro 3D (v4.4.4) and segmented/visualised in Avizo (v2019.4, Thermo-Fisher Scientific, USA).

Inductively coupled plasma-optical emission spectroscopy (ICP-OES)

Elemental analysis of transition metal concentrations in the positive electrodes was carried out using inductively coupled plasma-optical emission spectroscopy (ICP-OES, PerkinElmer), calibrated with high-purity standards (Choice Analytical). Electrode coatings were scraped from the current collectors and soaked in 4 mL of ultra-pure nitric acid (70%) for 12 hours, followed by the addition of 2 mL of ultra-pure hydrochloric acid (32%). The samples were then digested at 165 °C for 20 minutes using microwave digestion (Anton Paar) and subsequently diluted to a final volume of 14 mL with Milli-Q water (18.2 MΩ cm) for analysis.

Results & discussion

Characterisation of the electrode materials and cells

A dry 225 mAh sodium-ion pouch cell (Li-Fun Technology) was disassembled, and the electrodes were analysed. Synchrotron XRD patterns of each electrode shown in Fig. S2 determined that the positive electrode was layered and the negative electrode was hard carbon. Inductively Coupled Plasma (ICP) analysis confirmed that the positive electrode was composed of $NaMn_{0.39}Fe_{0.31}Ni_{0.22}Zn_{0.08}O_2$. Scanning Electron Microscopy (SEM) of the positive electrode revealed densely packed single crystal particles with average sizes ranging from 0.5 to 5 μm (Fig. S3). The particles displayed irregular, angular morphologies with relatively uniform distribution, indicative of a well-synthesised layered oxide structure. The SEM images of hard carbon (Fig. S4) displayed aggregated spherical particles with diameters in the range of ~0.5–3 μm. The particles exhibit irregular morphology with a rough, porous texture; their dense packing and visible interparticle voids suggest a disordered microstructure.

Acoustic emission and gassing during formation

Acoustic Emission (AE) detects gassing and cracking events inside batteries during formation cycles, arising from chemical and physical processes. The number of AE signals can be correlated with peaks in the differential capacity (dQ/dV) measurements. Fig. 2 shows this relationship for each electrolyte additive, using full three-electrode cell data from
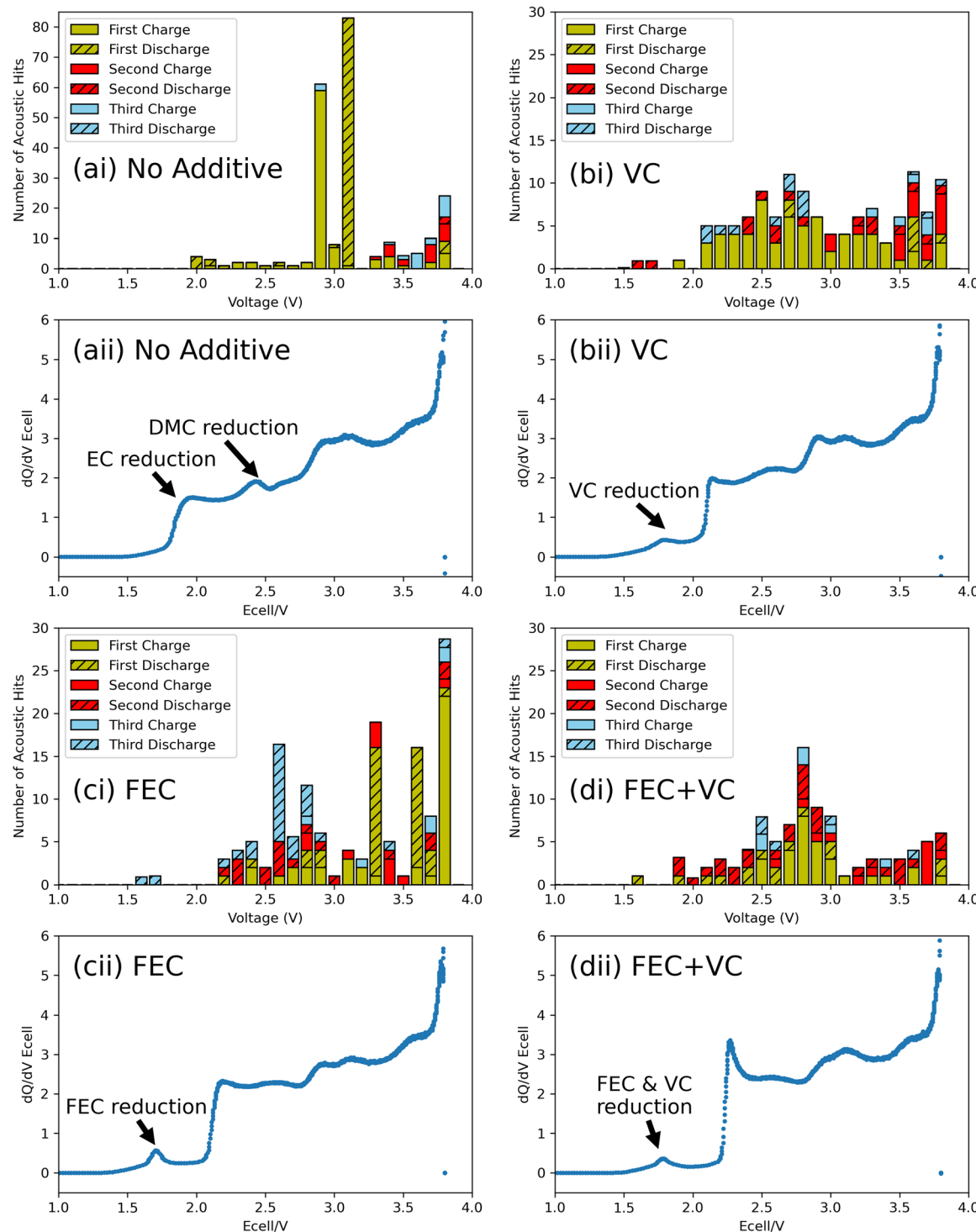
Fig. 2 AE histogram and dQ/dV plots. (ai, bi, ci and di) Number of AE hits for each charge/discharge process plotted against cell voltage in 0.1 V divisions. (aii, bii, cii and dii): dQ/dV from the C/20 formation cycle plotted against cell voltage. (a) No additive cell. (b) VC additive cell. (c) FEC additive cell. (d) VC and FEC additive cell for the first cycle. The dQ/dV data extracted from full-three electrode cell measurements using the same electrodes and electrolyte additives as the full pouch cells. The dQ/dV from the full pouch cells are shown in the SI (Fig. S8).

EL-CELL PAT-Cells alongside pouch cell data shown in Fig. S8. Additional dQ/dV results for the hard carbon electrode are displayed in Fig. S12. The dQ/dV subplots capture the reduction behaviour of each additive during SEI for-

mation, specific to the electrolyte composition. Only the first charging segment of the formation-cycle dQ/dV curve is shown to emphasise reduction peaks; complete curves are provided in Fig. S7.

For the 'no additive' cell containing 1 : 1 EC : DMC, there are three peaks at 1.93 V, 2.41 V and a split peak between 2.92–3.1 V. In the hard carbon electrode dQ/dV vs. Na/Na$^+$, corresponding peaks appear at 0.98 V and 0.6 V, but no third peak is present. The first two peaks match those observed in the full cell, indicating EC reduction at 1.93 V and a peak at 2.41 V, which is tentatively assigned to DMC reduction. This assignment is consistent with literature, where EC is known to reduce before DMC (voltage difference of ~0.3–0.5 V) and form a more stable SEI.[44] The third peak is only present in the positive electrode dQ/dV, suggesting it corresponds to continued sodium deintercalation and reactions at the positive electrode. For the VC additive cell, a broader peak at 1.77 V (1 V vs. Na/Na$^+$), attributed to VC reduction as it is a known SEI forming additive.[45] A following sharper peak at 2.25 V and a shallow peak at 2.65 V are seen in the full cell, which correspond to sodium intercalation in the hard carbon and further EC and DMC reduction. These three peaks also appear in the hard carbon electrode dQ/dV, indicating electrochemical processes on hard carbon, whereas a fourth peak at 2.85 V, is only present in the positive electrode dQ/dV (Fig. S11).

In the FEC-containing electrolyte, a sharper first peak at 1.70 V (assigned FEC reduction) appears in the full cell and at 1.1 V vs. Na/Na$^+$ on the hard carbon negative electrode.[46] Additional peaks are observed at 2.28 V and 2.55 V, corresponding to sodium intercalation at the hard carbon electrode and solvent reduction. A split peak at 3–3.1 V is absent in the hard carbon electrode, but present in positive electrode dQ/dV. The combined VC + FEC additive cell shows a first reduction peak at 1.70 V, like FEC but broader and shallower, indicating a slower SEI formation requiring more charge over a wider voltage window. The second peak at 2.35 V is larger than observed in FEC and VC alone indicating a combined effect on reduction of EC. The results suggest VC and FEC accelerate SEI formation on the negative electrode, suppressing EC reduction and reducing charge transfer. Analysis of the dQ/dV during the second and third formation charges at C/5 (Fig. S1) shows a flat plateau in the potential region where peaks appeared in the first charge, indicating that most electrolyte reduction occurred in the first cycle.

Each of the top subfigures represents a histogram of the number of acoustic events observed at specific voltages in the full cell. The colour of each bar indicates when the event occurs: during the first charge or discharge cycle at C/20, or during the second and third charge or discharge cycles at C/5.

In the cell with no additives, most acoustic hits are observed during the formation cycle. A small number of events (15 AE events) occur during the first charge between 2.0–2.9 V, with a significant spike (~120 AE events) at ~2.9 V. The largest spike occurs during the first discharge, a pattern not seen in cells containing electrolyte additives. This observation, along with continued spikes in acoustic events during the second and third charge cycles, suggests that the SEI formed by the reduction of EC and DMC alone is less stable than that formed with other electrolyte formulations containing additives. This instability leads to ongoing electrolyte decomposition, imply-

ing that the SEI was unable to fully passivate the hard carbon negative electrode of the cells (incomplete passivation). The areas of the electrode not passivated by the SEI continue to react with the electrolyte, producing AE hits as a result.

In cells with VC, FEC, or VC + FEC additives, most acoustic events are concentrated in the first cycle, although some events are also observed during the second and third C/5 cycles. This indicates that even with additives, the hard carbon negative electrode remains difficult to fully passivate. For example, in the cell with FEC, no acoustic events are observed until after 2.2 V, corresponding to the most prominent peak in the dQ/dV.[46] Additionally, some acoustic events are observed at higher voltages, potentially due to gas evolution at the positive electrode sodium deintercalation, which align with observed dQ/dV peaks from the three electrode measurements (Fig. S2).

To confirm the origin of the acoustic events, operando gas measurements were recorded alongside the acoustic measurements during the formation cycle. Fig. 3(a–di) shows the amplitude of acoustic hits from the cells in red transparent dots, overlaid with a line for the cumulative number of events. Fig. 3(a–dii) displays the volume of gas generated in green and all subfigures are plotted with the cell voltage in blue for each of the four cell chemistries. Data from the repeat acoustic experiments showing similar results are shown in Fig. S3.

For all chemistries, many acoustic hits were detected during the first charge of the formation cycle, as expected. After 1100 minutes (top of first charge, 3.8 V), the cell with no additive registered 110 AE events, while cells containing VC, FEC, and a combination of VC + FEC recorded 62, 45, and 38 AE events, respectively. The three-electrode data shown in Fig. S4 provides the onset potential (vs. Na) for the hits on the hard carbon negative electrode. Hits are first observed at a higher potential vs. Na for the no additive cell: 1.1 V, relative to 0.75, 0.73 and 0.69 V for the cell containing VC, FEC and FEC + VC respectively.

Additionally, gas production after the first charge measured approximately 1.8 ml for the cell with no additive, 0.15 ml for the cell with VC, 0.55 ml for the cell with FEC, and 0.58 ml for the cell with both VC and FEC. This gas increase is expected during the initial charge, as it coincides with the formation of the SEI, a process known to generate gas through the reduction of electrolyte solvent and/or additives.[15] The gas volume trend during charge correlates closely with the cumulative AE events, hence the gas production is the likely origin of the observed AE activity. This close alignment indicates that the quantity of AE events reflects the number of gas-generation events, while higher-amplitude signals correspond to larger bubble coalescence or cracking processes. This demonstrates that both the quantity and strength of AE signals provide a direct operando signature of gas evolution during formation. On discharge, there is a spike in number of AE events for the cell containing no additive, without a significant change in volume. The distinct differences in the three-electrode data (Fig. S9 and S11) between the cell without additives and those with electrolyte additives suggest that the spike could likely originate from electrode expansion and cracking in the electrodes. Being the
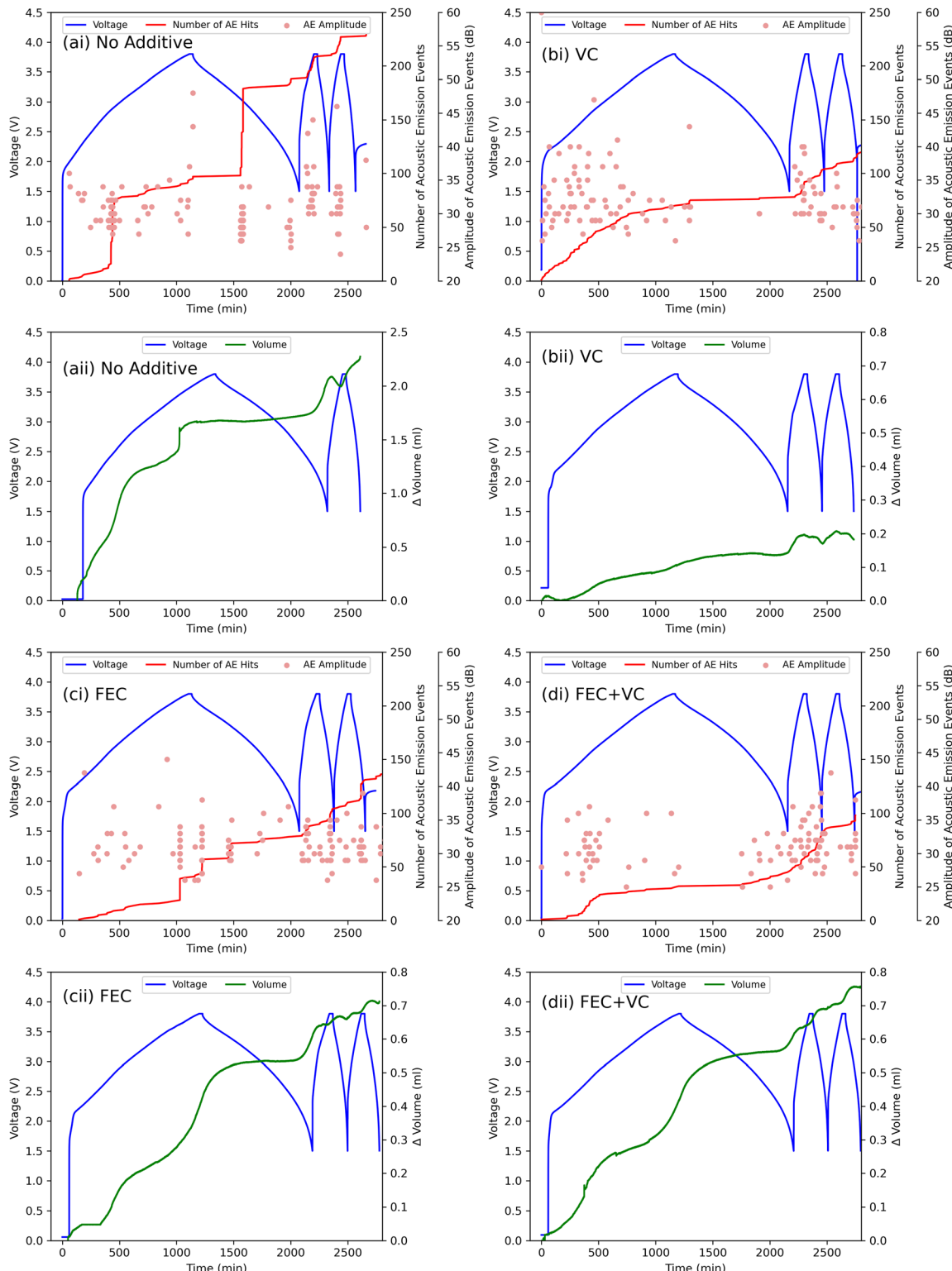
Fig. 3 Cell cycling data over C/20 formation cycle and C/5 diagnostic cycles. (ai, bi, ci and di) Amplitude of AE hits (red transparent dots) and Cumulative number of AE hits (red line) against cell voltage (blue line). (aii, bii, cii and dii) Change in cell volume against cell voltage. (a) No Additive cell. (b) VC additive cell. (c) FEC additive cell. (d) VC and FEC additive cell.

least stable configuration, it exhibits more AE events and generates significantly more gas than cells with electrolyte additives.

For all cell chemistries, the presence of acoustic hits, corresponding with spikes in gas volume, continued to occur after the initial formation cycle during the C/5 diagnostic cycles.

This behaviour is consistent with the reduced AE activity observed during the first C/20 discharge (Fig. 3bi), which generates minimal mechanical strain and gas evolution, and the subsequent increase in AE activity at C/5 where higher C-rates drive further interphase reactions. This observation contrasts with the behaviour observed in LIBs, for which far fewer acoustic events are typically recorded at this point since the SEI would have been fully passivated.[47,48] The high number of acoustic hits for all cells suggests that the SEI formation process is ongoing and that the initial film formed on hard carbon is poorly passivating compared to that on graphite negative electrodes in LIBs.[49]

Among the four electrolyte chemistries, the cell with no additive exhibited the highest number of AE events during the three formation cycles, with 256 events recorded, compared to 128 for the VC-containing cell, 142 for the FEC cell, and 109 for the FEC + VC cell, indicative of the absence of a sufficiently passivated SEI. This result is supported by the no additive cell producing by far the largest total amount of gas after the completion of three formation cycles (2.2 ml gas produced for no additive compared to 0.21 ml, 0.71 ml and 0.75 ml for VC, FEC, and VC + FEC respectively) and leads to the conclusion that an additive is needed for the formation of a stable SEI in these NIBs. The cell with the VC additive had the fewest acoustic hits recorded and produced the least gas. Interestingly, the cells containing both additives did not exhibit a combined effect; instead, they produced gas volumes similar to those in cells with only FEC. This result suggests gas evolution arises due to the presence of FEC rather than VC during SEI formation. Since FEC reduces at a lower full cell voltage than VC,[50–52] its reduction pathway likely causes gassing when the two additives are used together, which matches the observations in dQ/dV plots in Fig. 2. The results demonstrate that the frequency and timing of acoustic signals observed during formation and diagnostic cycles offer insights into the stability of the SEI on hard carbon and the overall performance of the cell. The signal strength also has practical significance because the amplitude of an AE event reflects the energy released during internal activity at the electrodes. These events, including bubble growth and crack formation, produce characteristic waveforms that correspond to distinct physical processes. As a result, both the amplitude and frequency of AE signals can be directly correlated with dynamic chemical behaviour such as SEI formation.

A limitation of using AE data is that it is not possible to determine if gassing occurs at the negative electrode or the positive electrode. However, more acoustic hits tend to be recorded at lower potentials, as shown by the three-electrode data, when the SEI is known to form, which causes gassing at the negative electrode. These hits correspond to a large spike in gas volume measurements at lower voltages in full cells. Some AE hits, coinciding with spikes in gas volume, are also recorded at higher voltages, likely due to positive electrode gassing reactions. This possible gassing at both electrodes aligns with literature,[26] and dips in gas volume measurements seen in the diagnostic cycles of the no additive and VC additive

cell could be due to gas consumption, as with reactions that occur in LIBs where CO_2 gas is consumed.[29] The observed gas consumption during discharge (Fig. 3aii–bii) arises from two likely effects: CO_2 dissolution into the electrolyte and its subsequent electrochemical reduction at the sodiated hard carbon surface.[26–29]

Alongside the passive AE, complementary active ultrasonic testing (UT) shows a strong correlation between the two techniques. UT measurements also identified the onset of gassing within the cell, evidenced by the loss of the pulse-echo signal,[53] as shown in Fig. S16 and S17. This loss of signal aligns with clusters of AE events, demonstrating the effectiveness of combining active and passive acoustic methods to noninvasively monitor cell behaviour. More details and explanations of the UT analysis are found in the SI.

X-ray CT also demonstrates the gassing that occurred during formation, with clear layer separation visible, further validating the origin of AE events. Analysis using 3D imaging software (Avizo) revealed that average electrode layer separation was greatest for the cell containing no additives and increased by ~22%.[54,55] More details are provided in the SI (Fig. S23).

Although *ex situ* techniques such as XPS or SEM could further verify SEI coverage, they are susceptible to artefacts from air exposure and beam damage. In contrast, our operando gas and acoustic diagnostics offer a reliable, real-time assessment of SEI integrity under electrochemical conditions. Future work will combine these measurements with controlled XPS, SEM, and online electrochemical mass spectrometry (OEMS) to directly link acoustic events with SEI morphology and chemistry. These findings demonstrate the value of acoustic techniques in identifying incomplete SEI formation and its underlying causes.

Machine learning waveform analysis

Following the analysis of the acoustic signals produced during the formation cycles of each electrolyte, common characteristic waveforms were identified across different electrolytes. Fig. 4 displays examples of the types of waveforms that are detected consistently throughout the formation process and are represented in both the time and frequency domains. The origin of these waveforms is likely to be caused by similar physical processes involved in SEI growth during the formation cycles. To gain a deeper understanding of these acoustic signals, an unsupervised machine learning (ML) framework was employed to categorise them based on their waveform properties.[16]

An unsupervised clustering approach using PCA and k-means was applied to classify AE waveforms, in a similar method to previous studies.[16] A set of multiple acoustic signal descriptors were standardised, and PCA was used to reduce the dataset to three dimensions while preserving as much variance as possible. The explained variance ratio for the first three principal components was calculated using Python's Scikit Learn library to assess the performance of PCA.

After dimensionality reduction, k-means clustering was applied to group the AE waveforms. The number of clusters, k,
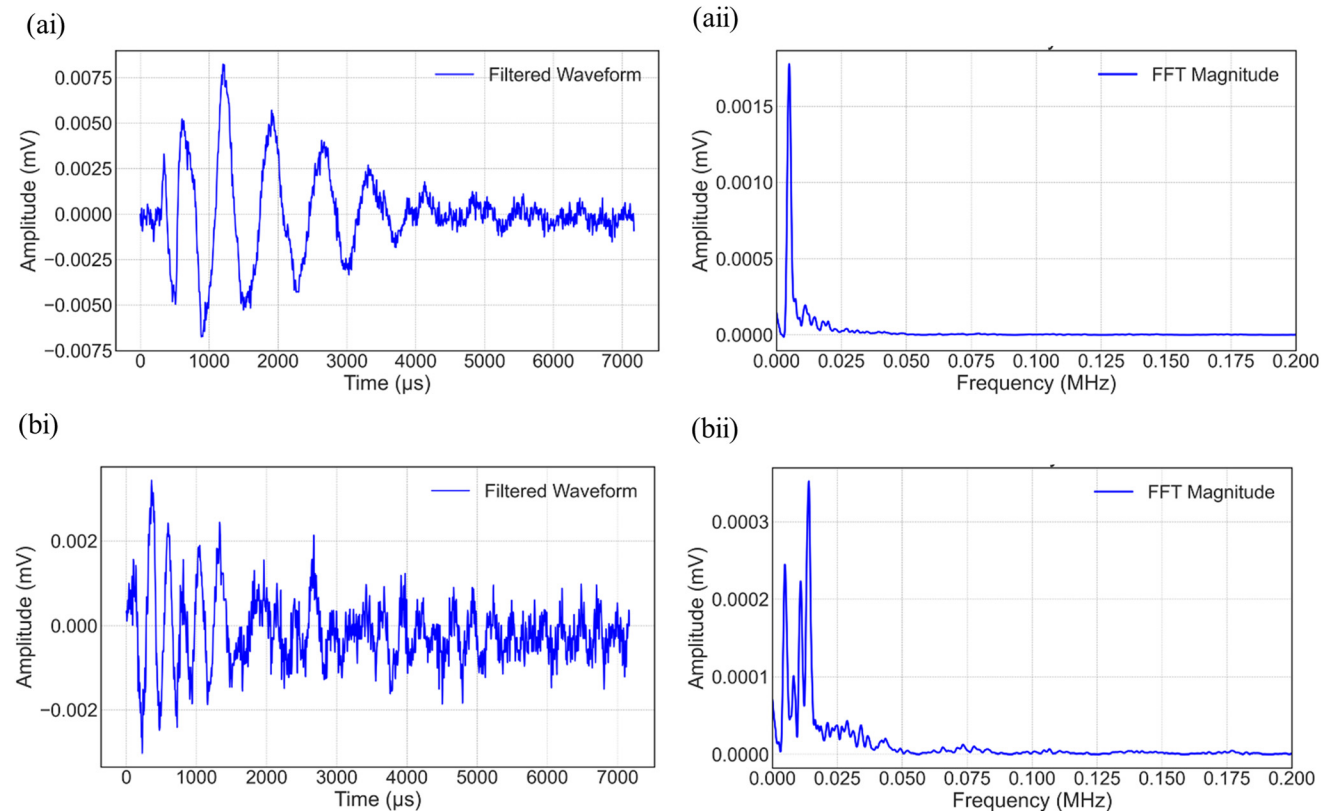
Fig. 4 Example waveforms in the time domain (ai & bi) and corresponding frequency components (aii & bii). Waveforms are extracted from the cell with no additive. (a) Displays a waveform produced during the first formation cycle and (b) produced later during discharge. Both signals are attributed to gassing within the cell.

was selected based on the silhouette score and visual analysis. The silhouette score, ranging from −1 to 1, measures how well data points fit within their clusters relative to others. Based on both quantitative and qualitative factors, $k = 4$ was chosen, as it provided distinct clusters while maintaining an optimal silhouette score.

The PCA analysis for all four cells (FEC, VC, FEC + VC) produced similar clustering results (Fig. 5). Notably, the cell with no additive in the electrolyte exhibited the highest number of AE signals, as shown in Fig. 3 compared to electrolytes containing additives. While k-means identified four clusters, the results indicate that most AE signals across all electrolytes shared common characteristics. The FEC additive showed the greatest variation in signal distribution, but overall, the clustering patterns suggest that the waveforms originated from similar sources. This supports the hypothesis that the signals were primarily generated by gassing during SEI formation and subsequent interphase reactions, as indicated by their predominance of lower-frequency components (<120 kHz) arising from gradual pressure changes during gas evolution, bubble nucleation, and coalescence, rather than the higher-frequency responses typical of cracking.[15] The raw acoustic signals used in this analysis are found in this public data repository: https://doi.org/10.5522/04/30392215.

Long-term electrochemical testing

The cells underwent 400 cycles between 1.5–3.8 V at C/3 (Fig. 6), with Electrochemical Impedance Spectroscopy (EIS) recorded every 50 cycles at three states of charge: 2.9 V, 3.3 V, and 3.7 V during rests upon charging (Fig. 7)[56] to minimise the effects of voltage slippage. Repeated long-term cycling experiments are shown in Fig. S20 and coulombic Efficiency data is shown in Fig. S7. These measurements were used to determine whether the behaviour observed during the formation stage was reflected in long-term performance. Impedance spectra were fitted using the ZFit function of the EC-Lab® software, with the equivalent circuit model (ECM) shown in Fig. S1. The selected ECM used consists of a series resistor ($R1$) followed by three R/CPE pairs ($R2/Q2 + R3/Q3 + R4/Q4$), representing SEI resistance (R_{SEI}), charge-transfer resistance (R_{CT}), and other interfacial or mass transfer processes. An additional CPE ($Q5$) accounts for low-frequency electrolyte diffusion. Representative EIS fits for cells containing various additives are presented in Fig. S8. A table of fitted $R2$, $R3$, $R4$ and R_{total} resistances for each measurement is shown in Table S1. Due to equipment limitations, PEIS spectra were collected starting from 10 kHz, omitting the high-frequency region (>10 kHz). While R_{SEI} was part of the analysis, the main focus was on the combined interfacial resistance ($R2 + R3 +$

a
Three PCA directions - No Additive
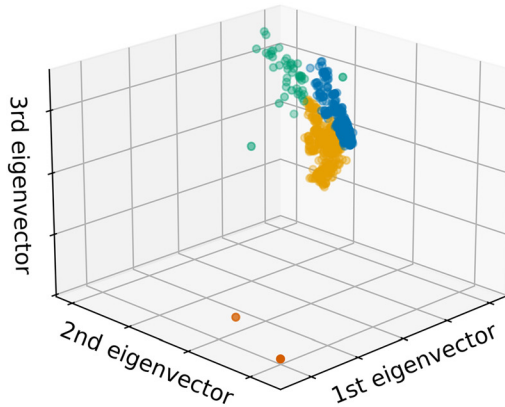
b
Three PCA directions - FEC
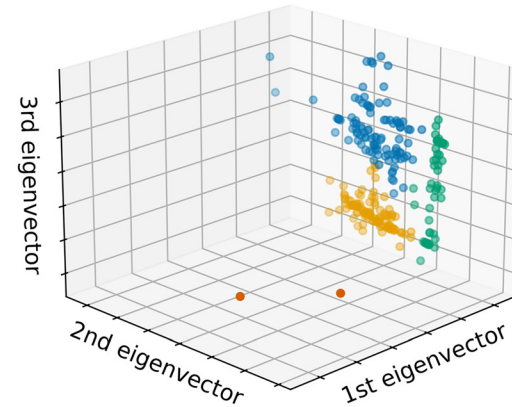
c
Three PCA directions - VC
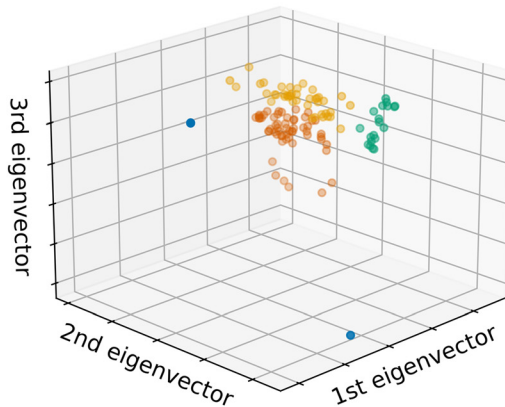
d
Three PCA directions - FEC + VC
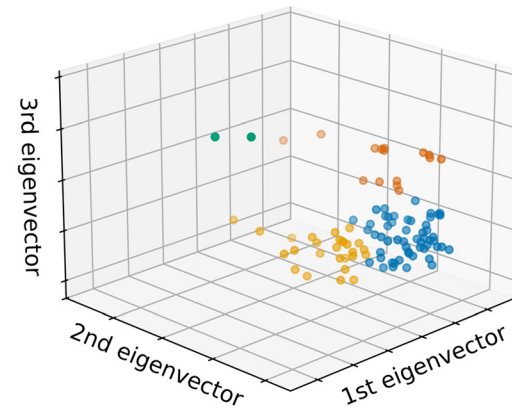
Fig. 5 3D plots showing k-means clustering results after applying PCA to the multi-dimensional acoustic features dataset. Each colour represents a different cluster. Each subfigure represents the results for each cell containing different electrolyte: (a) no additive (b) FEC (c) VC and (d) FEC + VC.

$R4$), as deconvolution of individual elements was hindered by overlapping time constants and missing high-frequency data. The $R1$ values remained largely constant at different voltages and throughout cell cycling.

The largest total combined resistance values were observed at 2.9 V for all electrolyte types used, with their lowest recorded resistance values at 3.3 V. This phenomenon can be explained by R_{CT}, and R_{SEI} values exhibiting an 'L'-shaped trend towards increasing SOC, consistent with previous studies.[57–59] Another common feature seen in the PEIS spectra of cells containing FEC, VC, and FEC + VC electrolyte additives (Fig. 7D–L) is the increased resistance at Cycle 0, which then decreases significantly and stabilises by Cycle 50.[56] This behavior can be attributed to the incomplete formation and passivation of the interfaces following the formation protocol and is further sup-

ported by the continuous gas evolution observed during AE testing for formation cycles 2 and 3. In addition, the observed changes in total resistance can also be influenced by the varying states of sodiation of both the positive and negative electrodes.

The smallest combined resistance was observed in the cell containing 5% FEC as the only additive. From the Nyquist plots for this electrolyte formulation collected at different voltage points and throughout cell cycling (Fig. 7G–I), a small semicircle growth can be observed from cycle 50 onward, indicating controlled interfacial growth and minimal increase in interfacial resistance over 400 cycles. This finding aligns with the capacity retention during cell cycling, as the cell containing 5% FEC as the sole additive maintained the highest capacity among all cells, reaching approximately 72% retention after 400 cycles (Fig. 6).
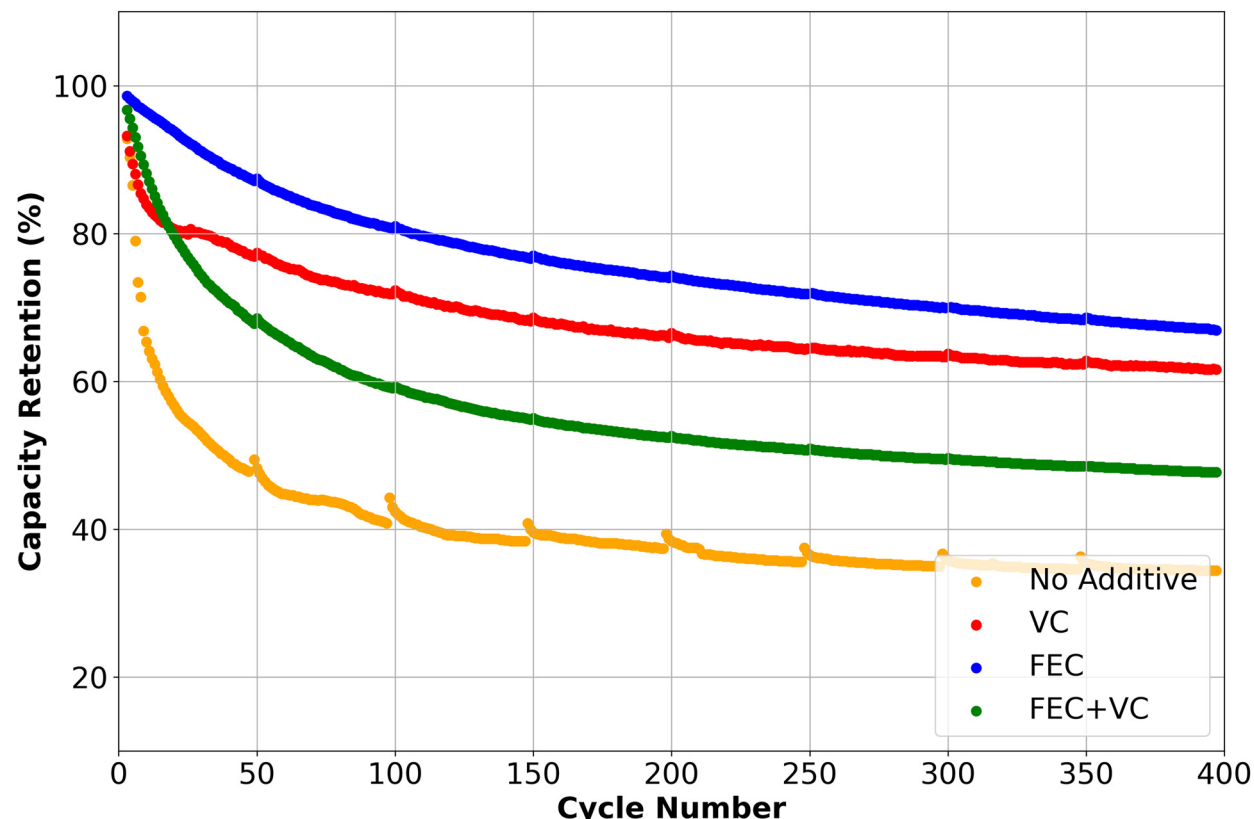
Fig. 6 Capacity retention for sodium-ion cells with different electrolytes (no additive, VC, FEC, FEC + VC). Cells were cycled at C/3 between 1.5–3.8 V for 400 cycles to assess the impact of electrolyte composition on long-term performance. Electrochemical Cycling repeats for each of these cells using the Novonix are shown in Fig. S20. coulombic Efficiency data is shown in Fig. S21.

In the case of a cell containing 5% VC electrolyte additive, a similar initial trend was observed. The R_{SEI} and the total combined resistance after formation (cycle 0) was relatively high (Fig. 7D–F), indicating incomplete passivation following formation. However, a significant drop in resistance occurred by cycle 50, and from that point onward, the resistance values steadily increased, indicating stabilisation of the interfacial layer. The gradual thickening of the SEI layer over time matches the capacity retention, which plateaued at approximately 63% after 400 cell cycles for the cell containing 5% VC electrolyte additive.

The cell containing a combination of FEC and VC additives showed the highest R_{SEI}, and the total combined resistance at different voltage points and throughout cell cycling (Fig. 7J–L). PEIS fitting confirmed a substantial resistance increase, with the total combined resistance value far exceeding those of cells containing individual additives. The discharge capacity dropped sharply during the first 80 cycles, after which it continued to decline more gradually, achieving and stabilising at approximately 59% capacity retention after 400 cell cycles. The combination of both additives likely promotes the formation of a thicker, more resistive SEI, as a broader range of organic species decompose. Consequently, the inferior performance of the FEC + VC electrolyte compared to the individual additives arises from the simultaneous decomposition of both com-

ponents, producing an over-passivated interphase that consumes additional sodium and hinders Na^+ transport, leading to increased impedance and reduced capacity retention. However, while this thickening results in the fastest growth of resistance compared to other cells, the capacity retention of this cell suggests that incorporating additives into the electrolyte remains beneficial over no additives, highlighting that a thicker, more resistive SEI layer does not always indicate a poor cell lifetime.

The Nyquist plots of the cell with no additive display clearly defined semicircles (Fig. 7A–C), suggesting the R_{CT} and R_{SEI}, processes are more dominant, suggesting either a well-developed or poorly conducting SEI layer, which impedes ionic transport across the interface. The same cell displayed the worst cycling performance, with capacity retention falling below 40% within the first 30 cycles, and continuing to decline thereafter (Fig. 6). Without electrolyte additives that help to improve electrode passivation, the resistances grow with cycle number at different voltages. The resulting impedance growth is consistent with continued electrolyte breakdown and poor surface passivation, explaining the severe capacity fade.

These findings support the hypothesis from the dQ/dV and formation analysis that additives influence SEI chemistry, and acoustics can detect ongoing SEI formation and the challenges of passivating hard carbon. Cells without additives showed
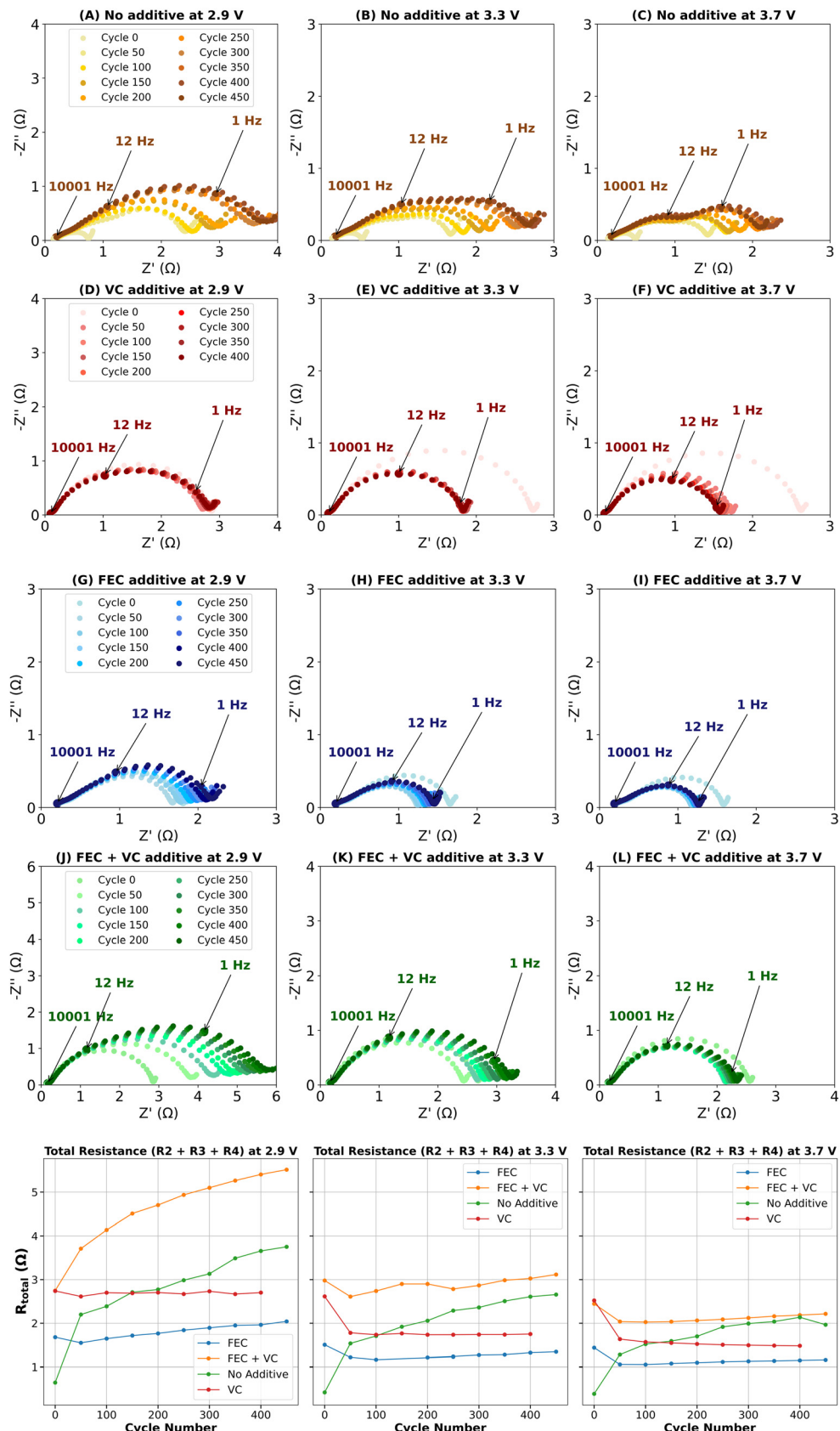
Fig. 7 Top figure displays EIS Nyquist plots and total fitted resistance ($R2 + R3 + R4$) for sodium-ion cells containing each electrolyte additives (No additive, VC, FEC, and VC + FEC) at 2.9 V, 3.3 V, and 3.7 V over cycling. EIS was measured every 50 cycles up to 450 cycles. Bottom figure shows the evolution of total fitted resistance fitted (R_{total}) with the equivalent circuit model (ECM) shown in Fig. S1.

poor performance, while VC or FEC individually improved cycling. However, their combination proved detrimental, highlighting the need for a carefully selected additive when using $NaPF_6$ in sodium-ion cells. It is noted that if the cells were cycled with a wider voltage range that the SEI behaviour could be different, due to the anode seeing more negative potentials. However, as noted in the methods and in Fig. S6, it was important to avoid significant transition metal dissolution at higher voltage in these cells, which could have skewed the SEI study. It is also important to note that these results were only validated at 25 °C, and the effect of various additives on SEI formation are expected to differ at more extreme temperatures. These effects will be the subject of future work, using the methods studied in the present work as a baseline.

Long-term acoustic emission testing

Following the formation cycle of each cell, additional AE experiments were conducted while the cells, containing different electrolytes, were cycled over 150 further cycles. Based on the capacity retention data, the worst-performing cell, which contained no additives, and the best-performing cell, containing FEC additive, were studied. The cell with no additive, which produced the most AE events and gas during formation, continued to generate AE events during long-term cycling (323 AE events) shown in Fig. S9. These AE events are attributed to ongoing interfacial reactions within the cell, consistent with the continued thickening and evolution of the SEI. This interpretation aligns with the EIS results, which show a progressive increase in interfacial impedance over cycling (Fig. 7). The sustained AE events during the first 50 cycles, during which capacity retention dropped to less than 60%, are indicative of degradation reactions occurring within the cell. In contrast, the cell containing FEC produced fewer AE events during formation, ~200 fewer in total relative to the cell without additive. In the subsequent 50 cycles, far fewer AE events were observed (54 AE events), consistent with the lower impedance and better performance. These long-term AE tests demonstrate that AE can serve as a valuable quality control tool and a diagnostic technique for assessing the state of health (SoH) of batteries containing different electrolytes.

Conclusions

This study demonstrates the effectiveness of acoustic techniques, combining passive acoustic emission (AE) and active ultrasonic testing (UT), as a low-cost, operando diagnostic for monitoring SEI formation in sodium-ion batteries (NIBs). Using $NaMn_{0.39}Fe_{0.31}Ni_{0.22}Zn_{0.08}O_2$/hard carbon cells with four electrolyte chemistries (1 M $NaPF_6$ in EC : DMC with FEC, VC, or both), key insights into SEI development were revealed. For all formulations, SEI formation remained incomplete after the initial formation protocol, indicated by ongoing acoustic activity, gas evolution, and irreversible capacity loss. Cells without additives showed poor capacity retention and unstable SEI, emphasising the critical role of additives. Long-term

testing identified FEC as the most effective additive, while VC offered less stability and the combination led to poorer performance.

These findings provide the first operando evidence that conventional formation protocols leave the SEI in NIBs incompletely developed, revealed through combined acoustic and gas diagnostics. The method is chemistry-agnostic, as acoustic signals arise from universal physical processes such as gassing and electrode strain. Demonstrated here for NIBs and previously for LIBs, it shows strong potential as a universal diagnostic tool. Using AE hits as a real-time metric for SEI stability can guide refined electrolyte formulations, reducing formation time and cost while improving manufacturing efficiency. In addition, the suppression of AE activity to a low and stable level provides an operando threshold for identifying when the SEI has effectively passivated the electrode surface. This drop in AE events indicates that major interfacial reactions and gas evolution have subsided and highlights the potential of AE monitoring to determine SEI completion during formation. Validated through gas analysis, EIS, and X-ray CT, this approach offers a practical alternative to traditional *ex situ* diagnostics and supports scalable, non-destructive monitoring. Future work will focus on industrial validation of these acoustic methods, addressing challenges of noise, sensor placement, and signal consistency through modular sensing, acoustic shielding, and advanced modelling.

Conflicts of interest

Authors A.F and R.J. are affiliated with AcouBatt Limited, and R.E.O, D.J.L.B, P.R.S and J.B.R. are affiliated with Sention Technologies Limited - companies with potential commercial interest in applications related to this study. The companies were not involved in the research present.

Data availability

Supporting data are provided in the supplementary information (SI). Supplementary information: additional experimental details, validation, and extended datasets. These include: synchrotron X-ray diffraction (XRD) patterns highlighting structural evolution; X-ray computed tomography (CT) reconstructions for morphological and volumetric analysis; electrochemical impedance spectroscopy (EIS) spectra and equivalent circuit fitting; gas volume analysis; dQ/dV measurement repeats to assess reproducibility and consistency; three-electrode electrochemical measurements for mechanistic insight; machine learning–based analysis for feature identification and correlation; acoustic emission repeats for gas and degradation monitoring; ultrasonic testing measurements to probe mechanical integrity; extended long-term electrochemical cycling data for stability assessment; detailed electrode architecture, composition, and fabrication parameters. Together, these datasets support the main findings and

provide comprehensive validation of the study and encompass all data used in this work. See DOI: https://doi.org/10.1039/d5eb00170f.

The raw acoustic signals used in the analysis are found in this public data repository: https://doi.org/10.5522/04/30392215

References

1 A. Mayyas, D. Steward and M. Mann, The case for recycling: Overview and challenges in the material supply chain for automotive li-ion batteries, *Sustainable Mater. Technol.*, 2019, **19**, e00087.

2 E. Pilali, F. F. Nia, E. Yamini, F. Esmaeilion, W. Alfraidi, A. Taklifi, D. A. Garcia and M. Soltani, *SWOT analysis on the transition from Lithium-Ion batteries to Sodium-Ion batteries, Sustainable Energy Technologies and Assessments*, 2025, **80**, 104371, DOI: 10.1016/j.seta.2025.104371.

3 A. Alessia, B. Alessandro, V. G. Maria, V. A. Carlos and B. Francesca, Challenges for sustainable lithium supply: A critical review, *J. Cleaner Prod.*, 2021, **300**, 126954, DOI: 10.1016/j.jclepro.2021.126954.

4 R. Rao, L. Chen, J. Su, S. Cai, S. Wang and Z. Chen, Issues and challenges facing aqueous sodium–ion batteries toward practical applications, *Battery Energy*, 2024, **3**, 20230036.

5 J.-Y. Hwang, S.-T. Myung and Y.-K. Sun, Sodium-ion batteries: present and future, *Chem. Soc. Rev.*, 2017, **46**, 3529–3614, DOI: 10.1039/C6CS00776G.

6 A. Rudola, C. J. Wright and J. Barker, Reviewing the Safe Shipping of Lithium-Ion and Sodium-Ion Cells: A Materials Chemistry Perspective, *Energy Mater. Adv.*, 2021, **2021**, 9798460, DOI: 10.34133/2021/9798460.

7 T. Song, B. Kishore, Y. Lakhdar, L. Chen, P. R. Slater and E. Kendrick, Effects of Storage Voltage upon Sodium-Ion Batteries, *Batteries*, 2024, **10**, 361.

8 J. B. Robinson, T. M. M. Heenan, J. R. Jervis, C. Tan, E. Kendrick, D. J. L. Brett and P. R. Shearing, Multiscale tomographic analysis of the thermal failure of NIB, *J. Power Sources*, 2018, 360–368, DOI: 10.1016/j.jpowsour.2018.07.098.

9 J. B. Robinson, D. P. Finegan, T. M. M. Heenan, K. Smith, E. Kendrick, D. J. L. Brett and P. R. Shearing, Microstructural Analysis of the Effects of Thermal Runaway on Li-Ion and Na-Ion Battery Electrodes, *J. Electrochem. Energy Convers. Storage*, 2018, **15**, 011010.

10 F. Schomburg, B. Heidrich, S. Wennemar, R. Drees, T. Roth, M. Kurrat, H. Heimes, A. Jossen, M. Winter and J. Y. Cheong, Lithium-ion battery cell formation: status and future directions towards a knowledge-based process design, *Energy Environ. Sci.*, 2024, DOI: 10.1039/d3ee03559j.

11 S. J. An, J. Li, Z. Du, C. Daniel and D. L. Wood III, Fast formation cycling for lithium ion batteries, *J. Power Sources*, 2017, **342**, 846–852, DOI: 10.1016/j.jpowsour.2017.01.011.

12 J. O. Majasan, J. B. Robinson, R. E. Owen, M. Maier, A. N. P. Radhakrishnan, M. Pham, T. G. Tranter, Y. Zhang, P. R. Shearing and D. J. L. Brett, Recent advances in acoustic diagnostics for electrochemical power systems, *JPhys Energy*, 2021, **3**, 032011, DOI: 10.1088/2515-7655/abfb4a.

13 T. Matsuo, M. Uchida and H. Cho, Development of Acoustic Emission Clustering Method to Detect Degradation of Lithium Ion Batteries, *J. Solid. Mech. Mater. Eng.*, 2011, **5**, 678–689, DOI: 10.1299/jmmp.5.678.

14 N. Beganovic and D. Söffker, Estimation of remaining useful lifetime of lithium-ion battery based on acoustic emission measurements, *J. Energy Resour. Technol.*, 2019, **141**, 041901.

15 C. Y. Choe, W. S. Jung and J. W. Byeon, Damage evaluation in lithium cobalt oxide/carbon electrodes of secondary battery by acoustic emission monitoring, *Mater. Trans.*, 2015, **56**, 269–273, DOI: 10.2320/matertrans.M2014396.

16 A. Fordham, S.-B. Joo, R. E. Owen, E. Galiounas, M. Buckwell, D. J. L. Brett, P. R. Shearing, R. Jervis and J. B. Robinson, Investigating the Performance and Safety of Li-Ion Cylindrical Cells Using Acoustic Emission and Machine Learning Analysis, *J. Electrochem. Soc.*, 2024, **171**, 070521, DOI: 10.1149/1945-7111/ad59c9.

17 A. G. Hsieh, S. Bhadra, B. J. Hertzberg, P. J. Gjeltema, A. Goy, J. W. Fleischer and D. A. Steingart, Electrochemical-

acoustic time of flight: In operando correlation of physical dynamics with battery charge and health, *Energy Environ. Sci.*, 2015, **8**, 1569–1577, DOI: 10.1039/c5ee00111k.

18 C. Bommier, W. Chang, J. Li, S. Biswas, G. Davies, J. Nanda and D. Steingart, Operando Acoustic Monitoring of SEI Formation and Long-Term Cycling in NMC/SiGr Composite Pouch Cells, *J. Electrochem. Soc.*, 2020, **167**, 020517, DOI: 10.1149/1945-7111/ab68d6.

19 X. Guo, S. Guo, C. Wu, J. Li, C. Liu and W. Chen, Intelligent Monitoring for Safety-Enhanced Lithium-Ion/Sodium-Ion Batteries, *Adv. Energy Mater.*, 2023, **13**, 2203903, DOI: 10.1002/aenm.202203903.

20 Z. Deng, Z. Huang, Y. Shen, Y. Huang, H. Ding, A. Luscombe, M. Johnson, J. E. Harlow, R. Gauthier and J. R. Dahn, Ultrasonic Scanning to Observe Wetting and Unwetting in Li ion Pouch Cells, *Joule*, 2020, **4**, 2017–2029, DOI: 10.1016/j.joule.2020.07.014.

21 Y. S. Zhang, A. N. Radhakrishnan, J. B. Robinson, R. E. Owen, T. G. Tranter, E. Kendrick, P. R. Shearing and D. J. L. Brett, In Situ Ultrasound Acoustic Measurement of the Lithium-Ion Battery Electrode Drying Process, *ACS Appl. Mater. Interfaces*, 2021, **13**, 36605–36620, DOI: 10.1021/acsami.1c10472.

22 S. L. Dreyer, R. Zhang, J. Wang, A. Kondrakov, Q. Wang, T. Brezesinski and J. Janek, The effect of configurational entropy on acoustic emission of P2-type layered oxide cathodes for sodium-ion batteries, *JPhys Energy*, 2023, **5**, 035002.

23 S. Schweidler, S. L. Dreyer, B. Breitung and T. Brezesinski, Acoustic Emission Monitoring of High-Entropy Oxyfluoride Rock-Salt Cathodes during Battery Operation, *Coatings*, 2022, **12**, 402.

24 R. Mogensen, D. Brandell and R. Younesi, Solubility of the Solid Electrolyte Interphase (SEI) in Sodium Ion Batteries, *ACS Energy Lett.*, 2016, **1**, 1173–1178, DOI: 10.1021/acsenergylett.6b00491.

25 J. Song, B. Xiao, Y. Lin, K. Xu and X. Li, Interphases in Sodium-Ion Batteries, *Adv. Energy Mater.*, 2018, **8**, 1703082, DOI: 10.1002/aenm.201703082.

26 H. Hijazi, Z. Ye, E. Zsoldos, M. Obialor, W. Black, S. Azam, J. R. Dahn and M. Metzger, Can Layered Oxide/Hard Carbon Sodium-Ion Pouch Cells with Simple Electrolyte Additives Achieve Better Cycle Life than LFP/Graphite Cells?, *J. Electrochem. Soc.*, 2024, **171**, 050521, DOI: 10.1149/1945-7111/ad47da.

27 L. Zhang, C. Tsolakidou, S. Mariyappan, J.-M. Tarascon and S. Trabesinger, Unraveling gas evolution in sodium batteries by online electrochemical mass spectrometry, *Energy Storage Mater.*, 2021, **42**, 12–21, DOI: 10.1016/j.ensm.2021.07.005.

28 K. U. Schwenke, S. Solchenbach, J. Demeaux, B. L. Lucht and H. A. Gasteiger, The Impact of CO_2 Evolved from VC and FEC during Formation of Graphite Anodes in Lithium-Ion Batteries, *J. Electrochem. Soc.*, 2019, **166**, A2035–A2047, DOI: 10.1149/2.0821910jes.

29 L. D. Ellis, J. P. Allen, L. M. Thompson, J. E. Harlow, W. J. Stone, I. G. Hill and J. R. Dahn, Quantifying, Understanding and Evaluating the Effects of Gas Consumption in Lithium-Ion Cells, *J. Electrochem. Soc.*, 2017, **164**, A3518–A3528, DOI: 10.1149/2.0191714jes.

30 Z. Ye, H. Hijazi, W. Black, S. Azam, J. R. Dahn and M. Metzger, Impact of Salts and Linear Carbonates on the Performance of Layered Oxide/Hard Carbon Sodium-Ion Pouch Cells with Alkyl Carbonate Electrolytes, *J. Electrochem. Soc.*, 2024, **171**, 040522, DOI: 10.1149/1945-7111/ad3b73.

31 H. Yang, J. Hwang, Y. Tonouchi, K. Matsumoto and R. Hagiwara, Sodium difluorophosphate: facile synthesis, structure, and electrochemical behavior as an additive for sodium-ion batteries, *J. Mater. Chem. A*, 2021, **9**, 3637–3647, DOI: 10.1039/d0ta11689k.

32 D. Y. Wang, N. N. Sinha, J. C. Burns, C. P. Aiken, R. Petibon and J. R. Dahn, A Comparative Study of Vinylene Carbonate and Fluoroethylene Carbonate Additives for $LiCoO_2$/Graphite Pouch Cells, *J. Electrochem. Soc.*, 2014, **161**, A467–A472, DOI: 10.1149/2.001404jes.

33 L. Madec, R. Petibon, J. Xia, J.-P. Sun, I. G. Hill and J. R. Dahn, Understanding the Role of Prop-1-ene-1,3-Sultone and Vinylene Carbonate in $LiNi_{1/3}Mn_{1/3}Co_{1/3}O_2$/Graphite Pouch Cells: Electrochemical, GC-MS and XPS Analysis, *J. Electrochem. Soc.*, 2015, **162**, A2635–A2645, DOI: 10.1149/2.0741512jes.

34 R. Petibon, E. C. Henry, J. C. Burns, N. N. Sinha and J. R. Dahn, Comparative Study of Vinyl Ethylene Carbonate (VEC) and Vinylene Carbonate (VC) in $LiCoO_2$/Graphite Pouch Cells Using High Precision Coulometry and Electrochemical Impedance Spectroscopy Measurements on Symmetric Cells, *J. Electrochem. Soc.*, 2014, **161**, A66–A74, DOI: 10.1149/2.030401jes.

35 Y. Wang, C. Wang, Y. Wang, H. Liu and Z. Huang, Boric Acid Assisted Reduction of Graphene Oxide: A Promising Material for Sodium-Ion Batteries, *ACS Appl. Mater. Interfaces*, 2016, **8**, 18860–18866, DOI: 10.1021/acsami.6b04774.

36 L. O. Vogt, M. El Kazzi, E. J. Berg, S. P. Villar, P. Novák and C. Villevieille, Understanding the interaction of the carbonates and binder in Na-ion batteries: A combined bulk and surface study, *Chem. Mater.*, 2015, **27**, 1210–1216, DOI: 10.1021/cm5039649.

37 H. Shin, J. Park, A. M. Sastry and W. Lu, Effects of Fluoroethylene Carbonate (FEC) on Anode and Cathode Interfaces at Elevated Temperatures, *J. Electrochem. Soc.*, 2015, **162**, A1683–A1692, DOI: 10.1149/2.0071509jes.

38 L. Chen, B. Kishore, M. Walker, C. E. J. Dancer and E. Kendrick, Nanozeolite ZSM-5 electrolyte additive for long life sodium-ion batteries, *Chem. Commun.*, 2020, **56**, 11609–11612, DOI: 10.1039/d0cc03976d.

39 J. Fondard, E. Irisarri, C. Courrèges, M. R. Palacin, A. Ponrouch and R. Dedryvère, SEI Composition on Hard Carbon in Na-Ion Batteries After Long Cycling: Influence of Salts ($NaPF_6$, NaTFSI) and Additives (FEC, DMCF), *J. Electrochem. Soc.*, 2020, **167**, 070526, DOI: 10.1149/1945-7111/ab75fd.

40 C. P. Aiken, J. Xia, D. Y. Wang, D. A. Stevens, S. Trussler and J. R. Dahn, An Apparatus for the Study of In Situ Gas

Evolution in Li-Ion Pouch Cells, *J. Electrochem. Soc.*, 2014, **161**, A1548–A1554, DOI: 10.1149/2.0151410jes.

41 J. Self, C. P. Aiken, R. Petibon and J. R. Dahn, Survey of Gas Expansion in Li-Ion NMC Pouch Cells, *J. Electrochem. Soc.*, 2015, **162**, A796–A802, DOI: 10.1149/2.0081506jes.

42 C. P. Aiken, J. Self, R. Petibon, X. Xia, J. M. Paulsen and J. R. Dahn, A Survey of In Situ Gas Evolution during High Voltage Formation in Li-Ion Pouch Cells, *J. Electrochem. Soc.*, 2015, **162**, A760–A767, DOI: 10.1149/2.0941504jes.

43 M. T. M. Pham, J. J. Darst, D. P. Finegan, J. B. Robinson, T. M. M. Heenan, M. D. R. Kok, F. Iacoviello, R. Owen, W. Q. Walker, O. V. Magdysyuk, *et al.*, Correlative Acoustic Time-Of-Flight Spectroscopy and X-ray Imaging to Investigate Gas-Induced Delamination in Lithium-Ion Pouch Cells during Thermal Runaway, *J. Power Sources*, 2020, DOI: 10.1016/j.jpowsour.2020.228039.

44 I. Azcarate, W. Yin, C. Méthivier, F. Ribot, C. Laberty-Robert and A. Grimaud, Assessing the Oxidation Behavior of EC: DMC Based Electrolyte on Non-Catalytically Active Surface, *J. Electrochem. Soc.*, 2020, **167**, 080530, DOI: 10.1149/1945-7111/ab8f57.

45 Y. Qian, C. Schultz, P. Niehoff, T. Schwieters, S. Nowak, F. M. Schappacher and M. Winter, Investigations on the electrochemical decomposition of the electrolyte additive vinylene carbonate in Li metal half cells and lithium ion full cells, *J. Power Sources*, 2016, **332**, 60–71, DOI: 10.1016/j.jpowsour.2016.09.100.

46 X. Song, X. Zhou, Y. Zhou, Y. Deng, T. Meng, A. Gao, J. Nan, D. Shu and F. Yi, Reaction Mechanisms of Sodium-Ion Batteries under Various Charge and Discharge Conditions in a Three-Electrode Setup, *ChemElectroChem*, 2018, **5**, 2475–2481, DOI: 10.1002/celc.201800387.

47 A. Tranchot, A. Etiemble, P.-X. Thivel, H. Idrissi and L. Roue, *In situ* acoustic emission study of Si-based electrodes for lithium-ion batteries, *J. Power Sources*, 2015, 259–266, DOI: 10.1016/j.jpowsour.2014.12.126.

48 N. Kircheva, P.-X. Thivel, S. Genies, D. Brun-Buisson and Y. Bultel, Study of SEI Formation in Li-Ion Batteries by Acoustic Emission Technique, *ECS Trans.*, 2011, **35**, 19–26, DOI: 10.1149/1.3644900.

49 A. Bouibes, N. Takenaka, K. Kubota, S. Komaba and M. Nagaoka, Development of advanced electrolytes in Na-ion batteries: Application of the Red Moon method for molecular structure design of the SEI layer, *RSC Adv.*, 2022, **12**, 971–984, DOI: 10.1039/d1ra07333h.

50 Z. X. Huang, X. L. Zhang, X. X. Zhao, Y. Y. Zhao, V. Aravindan, Y. H. Liu, H. Geng and X. L. Wu, Electrode/electrolyte additives for practical sodium-ion batteries: a mini review, *Inorg. Chem. Front.*, 2022, DOI: 10.1039/d2qi02237k.

51 S. Komaba, T. Ishikawa, N. Yabuuchi, W. Murata, A. Ito and Y. Ohsawa, Fluorinated ethylene carbonate as electrolyte additive for rechargeable Na batteries, *ACS Appl. Mater. Interfaces*, 2011, **3**, 4165–4168, DOI: 10.1021/am200973k.

52 M. Hashimov and A. Hofmann, Deciphering Electrolyte Degradation in Sodium-Based Batteries: The Role of Conductive Salt Source, Additives, and Storage Condition, *Batteries*, 2023, **9**, 530.

53 A. Fordham, Z. Milojevic, E. Giles, W. Du, R. E. Owen, S. Michalik, P. A. Chater, P. K. Das, P. S. Attidekou, S. M. Lambert, *et al.*, Correlative non-destructive techniques to investigate aging and orientation effects in automotive Li-ion pouch cells, *Joule*, 2023, **7**, 2622–2652, DOI: 10.1016/j.joule.2023.10.011.

54 T. Krause, D. Nusko, L. P. Bauermann, M. Vetter, M. Schäfer and C. Holly, Methods for Quantifying Expansion in Lithium-Ion Battery Cells Resulting from Cycling: A Review, *Energies*, 2024, **17**, DOI: 10.3390/en17071566.

55 A. Wade, A. V. Llewellyn, T. M. M. Heenan, C. Tan, D. J. L. Brett, R. Jervis and P. R. Shearing, First Cycle Cracking Behaviour Within Ni-Rich Cathodes During High-Voltage Charging, *J. Electrochem. Soc.*, 2023, **170**, 070513, DOI: 10.1149/1945-7111/ace130.

56 D. Ledwoch, L. Komsiyska, E. M. Hammer, K. Smith, P. R. Shearing, D. J. L. Brett and E. Kendrick, Determining the electrochemical transport parameters of sodium-ions in hard carbon composite electrodes, *Electrochim. Acta*, 2022, **401**, 139481.

57 F. Linsenmann, D. Pritzl and H. A. Gasteiger, A Reference Electrode for In Situ Impedance Measurements in Sodium-Ion Batteries, *J. Electrochem. Soc.*, 2019, **166**, A3668–A3674, DOI: 10.1149/2.0741915jes.

58 M. Hess, Non-linearity of the solid-electrolyte-interphase overpotential, *Electrochim. Acta*, 2017, **244**, 69–76, DOI: 10.1016/j.electacta.2017.05.017.

59 Y. Chen, J. Key, K. O'Regan, T. Song, Y. Han and E. Kendrick, Revealing the rate-limiting electrode of lithium batteries at high rates and mass loadings, *Chem. Eng. J.*, 2022, **450**, 138275.